AGU100 ADVANCING EARTH AND SPACE SCIENCE

Check for updates

Radio Science

RESEARCH ARTICLE
10.1029/2019RS006793

Special Section:
URSI AT-RASC (Atlantic Radio Science Conference) 2018

Key Points:
- Propagation in extended anisotropic media has become important with the advent of global navigation satellites
- New configuration-space models are well suited for simulations
- An equivalent phase-screen model captures the structure and provides guidelines interpreting diagnostic measurements

Correspondence to:
C. Rino,
crino@bc.edu

Citation:
Rino, C., Carrano, C. S., & Groves, K. M. (2019). Wave field propagation in extended highly anisotropic media. *Radio Science*, *54*, 646–659. https://doi.org/10.1029/2019RS006793

Received 4 JAN 2019
Accepted 17 JUN 2019
Accepted article online 28 JUN 2019
Published online 22 JUL 2019

Wave Field Propagation in Extended Highly Anisotropic Media

Charles Rino[1], **Charles Carrano**[1], **and Keith Groves**[1]

[1]Institute for Scientific Research, Boston College, Boston, MA, USA

Abstract The theory propagation in the Earth's ionosphere is well established. However, with the advent of Global Navigation Satellite System measurements, new demands are being placed on satellite system performance evaluation and diagnostic measurements. Propagation simulations are essential for system performance evaluation and they provide guidelines for interpreting diagnostic measurements. This paper presents simulations of propagation in extended highly anisotropic media obtained with split-step integration of the parabolic wave equation. This requires three-dimensional realizations of the electron density structure. A new configuration-space model is used to generate realizations as summations of *striations*, which are local to field lines with defined scales and peak densities. The scale and peak densities can be selected to generate specified power law spectral density functions. An analytic three-dimensional expectation spectral density function provides a parameterized ionospheric structure model. The simulations results show that replacing the extended structure with an equivalent phase screen placed at the center of the structured region provides statistically equivalent realizations of observation-plane measurements at propagation distances greater than the layer extent. The equivalence is independent of the propagation direction relative to the magnetic field direction, although there is some variation for the extreme propagation disturbances caused by field-aligned propagation. We also investigate the interpretation of in situ and path-integrated diagnostic measurements and two-dimensional propagation models, which are being used to model diagnostic measurements directly.

1. Introduction

Although the theory of electromagnetic (EM) wave propagation in transparent media is well known, applications of the theory to performance evaluation of satellite communication, navigation, and surveillance systems are computationally intensive. An equivalent phase-screen model, which was introduced in the seminal paper by Booker et al. (1950), provides a simplified alternative. Even so, computational demands remain prohibitive for direct performance evaluation applications. More recently, Carrano and Rino (2016) developed a two-dimensional phase-screen theory and demonstrated a computationally efficient implementation. Such two-dimensional propagation models are attractive because the results can be applied directly to measured one-dimensional time series. As shown, for example, by Carrano et al. (2014), successful applications include backpropagation. However, Global Navigation Satellite System (GNSS) ionospheric diagnostics, particularly occultation measurements using receivers carried by low-orbiting satellites (Tsai et al., 2011), have placed new demands on propagation models.

This paper investigates EM propagation in extended highly anisotropic media with emphasis on validating phase-screen equivalence and the interpretation of diagnostic measurements. The study is based on complex field simulations generated by split-step integration of the parabolic wave equation (PWE). Structure realizations are constructed with a recently developed configuration-space model described in Rino et al. (2018). Configuration-space realizations are summations of physical *striations* with size and intensity distributions constrained to follow two-component inverse power law spectral density functions (SDFs).

Parameterized analytic SDF representations are effectively ionospheric structure models. The defining model parameters can be derived from diagnostic measurements with irregularity parameter estimation (IPE) procedures demonstrated in Carrano et al. (2017) and Rino and Carrano (2018). The results of this study show that phase-screen equivalence is surprisingly robust. Moreover, for all but extreme disturbances generated by field-aligned propagation, the dependence of the derived structure parameters on the propagation direction relative to the magnetic field can be accommodated with the same geometric scale correction factors that are used routinely for scintillation diagnostics.

To introduce the simulation procedure, we summarize the mathematical formulation of the propagation theory, which is compact and readily understood functionally. We let $\psi(x,\vec{\rho})$ represent the $[x,\vec{\rho}]$ position-dependent complex modulation imparted to a signal traversing the ionosphere. At GNSS frequencies, $\psi(x,\vec{\rho})$ is fully characterized by the PWE,

$$\frac{\partial\psi(x,\vec{\rho})}{\partial x}=\Theta_k\psi(x,\vec{\rho})+ik\Delta n(x,\vec{\rho})\psi(x,\vec{\rho}), \tag{1}$$

where $k = 2\pi f/c$, f is the frequency, and c is the velocity of light. The function $\Delta n(x,\vec{\rho})$ represents the refractive index. At GNSS frequencies,

$$k\Delta n(x,\vec{\rho})\approx-(2\pi K/f)\Delta N_e(x,\vec{\rho}), \tag{2}$$

where $K = 1.3454\times10^9\ \mathrm{m}^2/\mathrm{s}$, and $\Delta N_e(x,\vec{\rho})$ is the electron density variation per cubic meter. To simplify the notation, the frequency dependence of $\psi(x,\vec{\rho})$ is left implicit. Motion of the propagation path using an effective scan velocity relative to the structure converts point measurements to one-dimensional scans in the observation plane at x. Space-to-time conversion generates the observable time series

$$v(t)\propto\psi(x,\vec{\rho}_0-\vec{v}_{\mathrm{veff}}(t-t_0)). \tag{3}$$

The effective velocity $\vec{v}_{\mathrm{veff}}$ defines the motion of the propagation path relative to the structure with an anisotropy correction.

The leading term on the right-hand side of (1) is a propagation operator that advances the field in free space:

$$\Theta\psi\left(x;\vec{\rho}\right)=\int\int\hat{\psi}\left(x;\vec{\kappa}\right)\exp\left\{i(\kappa\rho_F)^2/2\right\}\exp\left\{i\vec{\rho}\cdot\vec{\kappa}\right\}\frac{d\vec{\kappa}}{(2\pi)^2} \tag{4}$$

where

$$\hat{\psi}\left(x;\vec{\kappa}\right)=\int\int\psi\left(x;\vec{\rho}\right)\exp\{-i\vec{\kappa}\cdot\vec{\rho}\}d\vec{\rho} \tag{5}$$

is the two-dimensional Fourier decomposition of the complex field in the plane at x. The Fresnel scale is defined as

$$\rho_F=\sqrt{x_p/k}, \tag{6}$$

where x_p is the propagation distance from x. The dependence of the propagation operator on the single parameter ρ_F is a consequence of the parabolic approximation

$$(k-k_x(\kappa))x_p=(k-\sqrt{1-(\kappa/k)^2})x_p \tag{7}$$

$$\approx-\kappa^2(x_p/k) \tag{8}$$

A derivation of (1) can be found in chapter 2 of Rino (2011). As the PWE is written here, the x axis is aligned with the propagation direction of the incident plane wave. For propagation geometries with the source well separated from the structured region, a standard scale correction accommodates wavefront curvature as described in Appendix A4 of Rino (2011).

The PWE can be integrated by specifying a starting field at $x = 0$ with sequential evaluation of the propagation and media interaction terms. This approach requires approximating the propagation operator. Alternatively, split-step integration first converts $ik\Delta n(x,\vec{\rho})\psi(x,\vec{\rho})\mathrm{d}x$ to a phase perturbation, which is applied to the field at the starting point of the current integration step. The propagation operator advances the phase-incremented field to the next plane without approximation to complete the integration step. Split-step integration and the multiple-phase-screen (MPS) method are procedurally identical. However, uncorrelated phase screens are often used in MPS simulations. Knepp (1983) showed that uncorrelated phase screens are well matched to the hierarchy of first-order differential equations that characterize the evolution of complex field moments in an extended medium (Tatarskii, 1971). No additional constraints are imposed on direct PWE solutions.

There are several global ionospheric models such as the International Reference Ionosphere (Bilitza & Reinisch, 2015) that characterize large-scale structure. Stochastic ionospheric structure models are most often embedded in scintillation models. The WBMOD scintillation model described by Secan et al. (1995) incorporates an empirical structure model. An equatorial scintillation model developed by Retterer (2010) combines an approximate analytic propagation model with inputs from a physics-based structure simulation. As will be discussed in the section 2, conventional realizations of ionospheric structure impose a specified SDF onto uncorrelated unit average intensity Fourier modes. Simulations that use numerical integration of the PWE with such realizations have been developed by Béniguel (2002) and Deshpande et al. (2014). A hybrid model that generates realizations from theoretical calculations of the complex field moments has been developed by Gherm et al. (2005), Zernov and Gherm (2015), and Gherm and Zernov (2015) with extensions to oblique geometries by Gherm and Zernov (2017). A model based on phase-screen simulations was developed by Ghafoori and Skone (2015).

Section 2 reviews the configuration-space model with specific identification of a three-dimensional ionospheric SDF structure model, which is used for interpreting diagnostic measurements as described in sections 3.2 and 3.3. The principal simulation results are presented in section 3.1.

2. Configuration-Space Realizations

A realization of electron density structure is an essential input for integrating the PWE. A standard method for generating three-dimensional electron density realizations imposes a specified three-dimensional SDF by appropriately weighting uncorrelated, unit variance, Fourier components:

$$\Delta N_e(x,\vec{\rho}) = \int\int\int \sqrt{\Phi_{\Delta N_e}\left(\kappa_x,\vec{\kappa}\right)}\varsigma\left(\kappa,\vec{\kappa}\right) \times \exp\left\{i\left(\kappa_x x + \vec{\kappa}\cdot\vec{\rho}\right)\right\}\frac{d\vec{\kappa}}{(2\pi)^2}\frac{d\kappa_x}{2\pi}. \tag{9}$$

The white noise correlation property of $\varsigma\left(\kappa_x,\vec{\kappa}\right)$ can be written formally as

$$\left\langle \varsigma\left(\kappa_x,\vec{\kappa}\right)\varsigma^*\left(\kappa_x',\vec{\kappa}'\right)\right\rangle = 2\pi\delta\left(\kappa_x-\kappa_x'\right)(2\pi)^2\delta\left(\vec{\kappa}-\vec{\kappa}'\right). \tag{10}$$

Direct computation will show that the expectation SDF of $\Delta N_e(x,\rho)$ as defined by (9) is $\Phi_{\Delta N_e}\left(\kappa_x,\vec{\kappa}\right)$. The realizations are zero mean and invariant to a reflection of the reference coordinate system, which are not properties of real ionospheric structure.

Following the development in Rino et al. (2018), a configuration-space realization of $\Delta N_e(x,\vec{\rho})$ is constructed as a summation of physical striations. Formally,

$$\Delta N(x,\vec{\rho}) = \frac{1}{N_s}\sum_{k=1}^{N_s} C_k\sigma_k^{\gamma_k}p_\perp\left(\sqrt{\left(s+\eta_{s_k}\right)^2+\left(t+\eta_{t_k}\right)^2}/\sigma_k\right), \tag{11}$$

The profile function $p_\perp(\tau)$ is 0 for $|\tau| > 1/2$ with $p_\perp(0) = 1$. Striations are defined in magnetic-field-aligned coordinates ςst, with ς measured along the magnetic field direction. Under the assumption that magnetic field lines are parallel in the realization volume, the $\varsigma = 0$ plane intercepts η_{s_k} and η_{t_k} locate the N_s contributing striations. The strength of each striation is determined by $C_k\sigma_k^{\gamma_k}$. The size of each striation is determined by σ_k. The functional dependence on $[x,\vec{\rho}]$ is obtained by rotating the field-aligned coordinates as follows:

$$\begin{bmatrix}\zeta\\ s\\ t\end{bmatrix} = \begin{bmatrix}0 & 0 & 0\\ c_{21} & c_{22} & c_{23}\\ c_{31} & c_{32} & c_{33}\end{bmatrix}\begin{bmatrix}x\\ y\\ z\end{bmatrix}. \tag{12}$$

The matrix elements c_{ij} are functions of the magnetic field direction angles in the reference coordinate system (see Appendix A). Rotating the data space coordinate system relative to the magnetic field introduces the dependence of $\psi(x,\vec{\rho})$ on the magnetic field direction. To the extent that the data volume captures the structure, rotating the data space gives results identical to accommodating the angle dependence in the PWE. The two complementary coordinate systems evolved from seminal papers by Budden (1964) and Briggs and Parkin (1962).

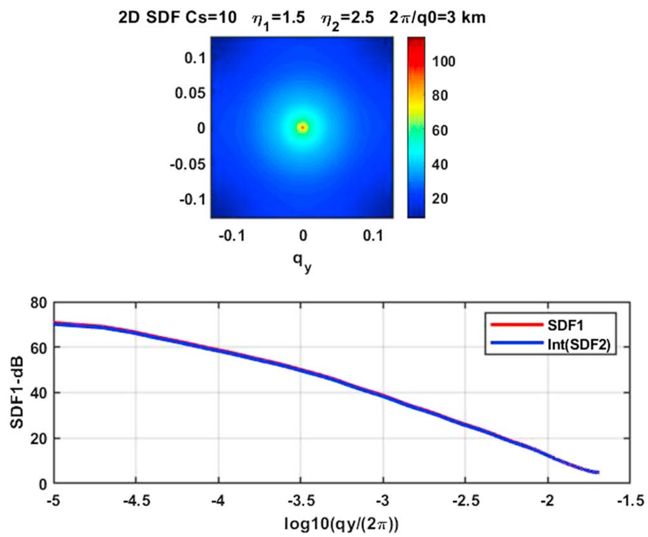

Figure 1. Upper frame shows the two-dimensional spectral density function (SDF) computed from (20) for the cross-field geometry. The lower frame shows the agreement of two calculations of the one-dimensional SDF.

As discussed in Rino et al. (2018), one two- or three-dimensional Fourier transformations of (11) can be computed analytically. Furthermore, for a uniform distribution of striations, the expectation SDF can also be computed. For example, the three-dimensional spectral density is defined by the relation

$$\Phi_{N_e}\left(\kappa_x,\vec{\kappa}\right)=\frac{1}{N_s}\sum_{j=1}^{J}C_j^2N_j^2\sigma_j^{2\gamma_k+(3-\epsilon(3))}\left|\int\int p_\perp\left(\sqrt{s^2+t^2}/\sigma_j\right)\exp\{-i(\vec{\kappa_s s+\kappa_t t})\}\mathrm{d}s\mathrm{d}t\right|^2 2\pi\delta\left(\kappa_\varsigma\right). \tag{13}$$

The spectral-domain coordinates in measurement and field-aligned spaces are related by the transpose of the C matrix in (12), whereby

$$\begin{bmatrix}\kappa_\varsigma\\ \kappa_s\\ \kappa_t\end{bmatrix}=\begin{bmatrix}0&0&0\\ c_{12}&c_{22}&c_{32}\\ c_{13}&c_{23}&c_{33}\end{bmatrix}\begin{bmatrix}\kappa_x\\ \kappa_y\\ \kappa_z\end{bmatrix}. \tag{14}$$

The reduced summation in (13) from N_s to J is a consequence of the bifurcation rule

$$\sigma_j=\sigma_{\max}2^{-(J-j)}j=1,2,\ldots,J \tag{15}$$

$$N_j=2^{d-J}. \tag{16}$$

Each group of N_j striations has the same size and intensity. The total number of striations is

$$N_s=\sum_{j=1}^{J}N_j. \tag{17}$$

The parameter $d>J$ is selected to provide a good approximation to the desired expectation SDF.

Because there is no variation along the magnetic field direction, the corresponding Fourier domain variation is concentrated at $\kappa_\varsigma=0$ as a delta function. This is a manifestation of the fact that the defining ionospheric SDF is two-dimensional. In Rino et al. (2018) numerical evaluation of the one-dimensional SDF,

$$\Phi^{(1)}_{N_e}\left(\kappa_y\right)=\frac{1}{N_s}\sum_{j=1}^{J}C_j^2N_j^2\sigma_j^{2\gamma_k+(3-\epsilon(1))}\left|\int p_\perp\left(s/\sigma_j\right)\exp\{-i\kappa_y y\}\mathrm{d}y\right|^2. \tag{18}$$

was used to show that with $\epsilon(1)=1$ and $\eta_n=2\gamma_n+2$, the configuration-space one-dimensional SDF closely approximates the desired two-component form

$$\Phi^{(1)}_{N_e}(q)\simeq C_s^{(1)}\begin{cases}q^{-\eta_1} & \text{for } q\le q_0\\ q_0^{\eta_2-\eta_1}q^{-\eta_2} & \text{for } q>q_0\end{cases}. \tag{19}$$

It is desirable to have a similar analytic form for the two-dimensional SDF $\Phi_{\Delta N_e}(\kappa_s,\kappa_t)$. We find that with $\epsilon(2)=2$ and $p_n=\eta_n+1$.

$$\Phi_{N_e}(\kappa)\simeq C_s^{(2)}\begin{cases}\kappa^{-p_1} & \text{for } \kappa\le\kappa_0\\ \kappa_0^{p_2-p_1}\kappa^{-p_2} & \text{for } \kappa>\kappa_0\end{cases}, \tag{20}$$

The general relation

$$\Phi^{(1)}(\kappa_y)=\int\Phi^{(2)}(\kappa_y,\kappa_z)\frac{d\kappa_z}{2\pi} \tag{21}$$

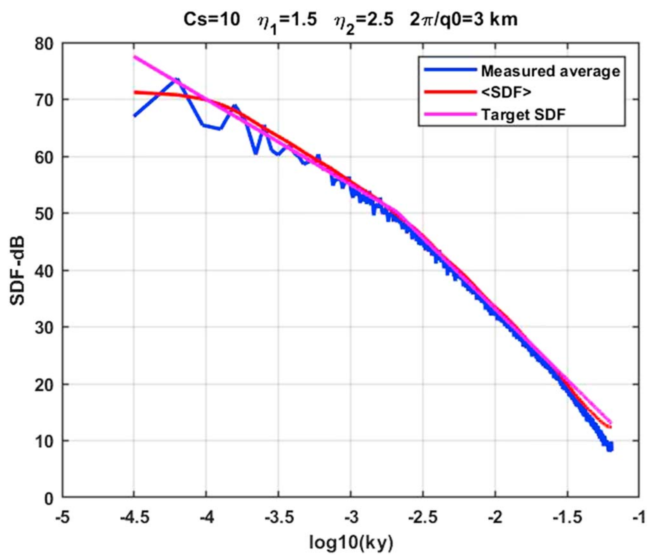

Figure 2. Measured average 1-D SDF (blue) with expectation 1-D SDF (red) and target 1-D SDF (magenta) overlaid. SDF = spectral density function.

was used to scale the turbulent strength parameters $C_s^{(2)}$ and $C_s^{(1)}$ consistently. The upper frame of Figure 1 shows a color intensity display of $\Phi_{N_e}(\kappa)$ as defined by (20) with the model parameters listed in the figure title. The lower frame is a comparison of the target one-dimensional SDF computed with (18) and the corresponding SDF computed by numerically evaluating (21) with the two-dimensional SDF defined by (20). The agreement verifies the observable and higher-dimensional model parameter relations. The power law index relation $p_n = \eta_n + 1$ is consistent with results for single power law SDFs.

The principal result in this section is (20), which upon using (14) becomes an ionospheric three-dimensional stochastic structure model. The model can be scaled to the observable one-dimensional model (19), which defines the configuration space parameters. The specific two-component model parameters are representative of the results from spectral analyses of high-resolution equatorial plasma bubble simulations reported by Rino et al. (2018).

3. Propagation Simulations

For this study configuration-space realizations with the defining parameters introduced in Rino et al. (2018) are used. Each realization is constructed from a set of $N_s = 8176$ striations covering $J = 9\,\sigma_j$ bifurcation levels from 50 km to 195.3 m. Figure 2 shows a measured average one-dimensional SDF (blue) from a realization, with the expectation SDF from (18) (red) and the target SDF from (19) (magenta) overlaid. Each realization populates a $30 \times 100 \times 50$ km volume with $128 \times 4,096 \times 4,096$ samples. As discussed in Rino et al. (2018), the generation of the electron density realization takes ≈30 min per layer. Parallel processing is used to reduce the overall computation time.

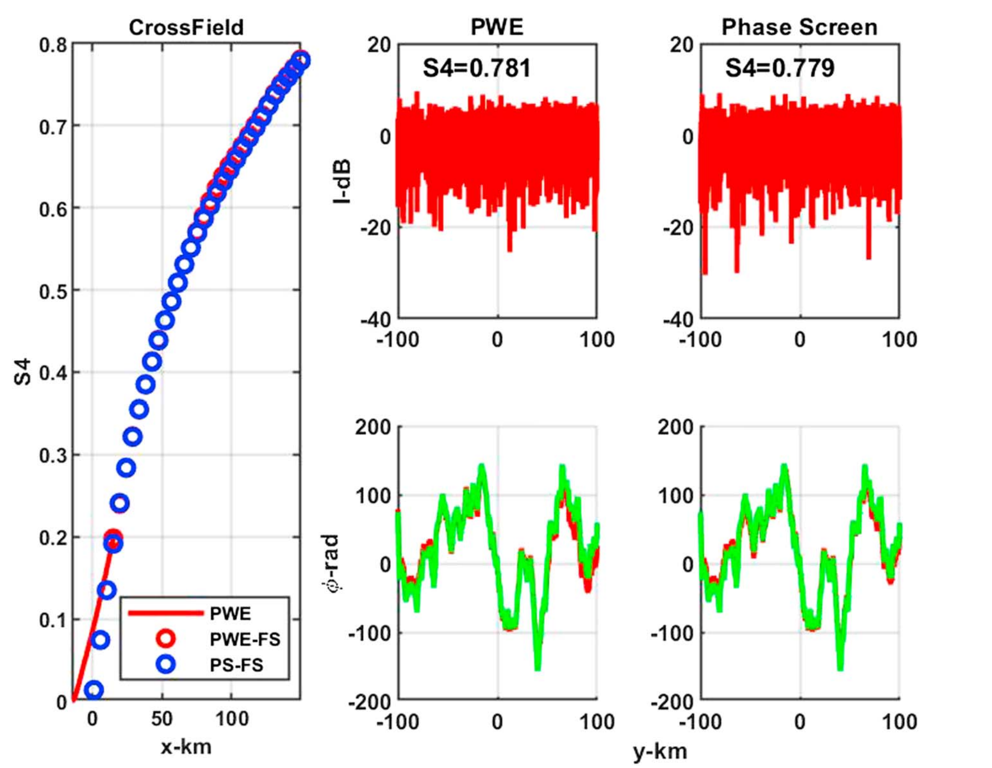

Figure 3. Cross-field summary. Left frame shows $S4$ for split step (red) and phase screen (blue). Middle and right frames show split-step and phase-screen intensity and phase from central observation-plane scan. The superimposed green curve is the path-integrated phase. PWE = parabolic wave equation.

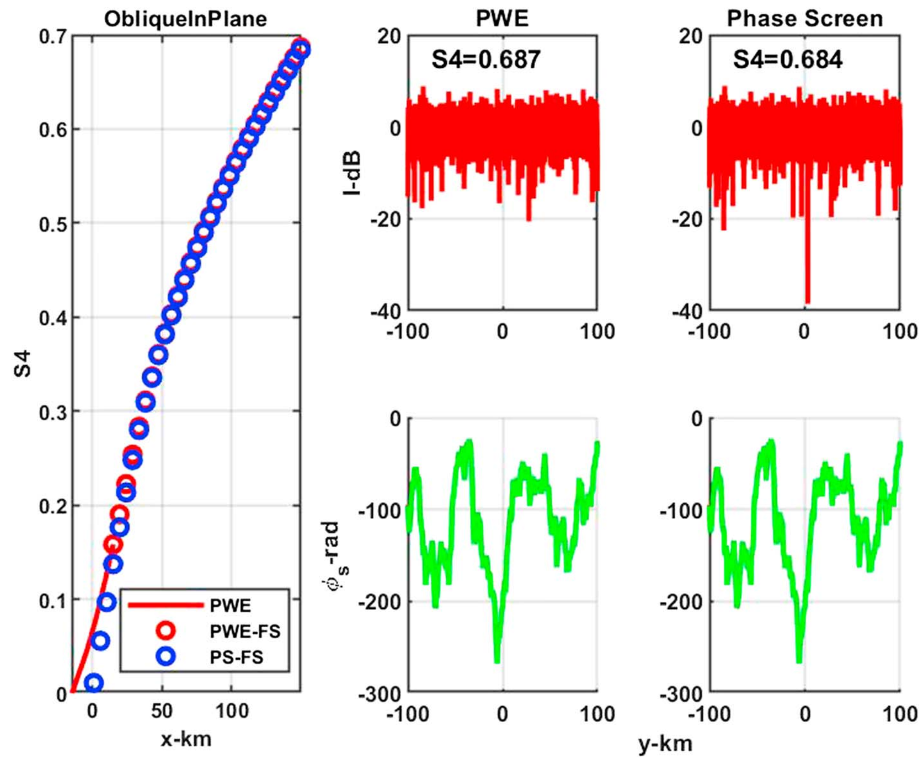

Figure 4. Oblique in-plane summary. Same format as Figure 3.

The size of the data volume was chosen to be large enough to represent intercepted GPS structure. With $C_s = 10$, strong GPS L1 frequency (1575.4 MHz) scintillation levels are generated in a measurement planes at $x = 150$ km. The distance was chosen to capture the fully developed scintillation. Structure is intercepted between $x = -15$ km and $x = 15$ km, whereby the nominal phase-screen propagation distance from the center of the region is $x = 150$ km.

For each realization split-step integration through the structured region as described in section 1 was performed followed by free-space propagation to $x = 150$ km. A second realization was constructed using the path-integrated phase applied at $x = 0$ to initiate an equivalent phase-screen simulation. The phase screen free-space propagation sampling was adjusted to coincide with the PWE free-space sampling for direct comparison.

Adequate sampling involves two considerations. Each integration step starts with an incremental phase change followed by free-space propagation, which imposes a corresponding incremental change in the intensity. The integration step size must be small enough to maintain small incremental complex field changes. Additionally, the Fourier transform sampling must be adequate to resolve the two-dimensional field structure. A stringent criterion is adequate sampling for unwrapping the multiple 2π jumps in the complex field phase angle. Algorithms for unwrapping two-dimensional complex phase fields are described in Ghiglia and Pritt (1998). One-dimensional unwrapping is a standard operation.

The path-integrated phase structure provides a good test for unwrapping because the initiating phase is known. For recovery of the path-integrated phase the $4,096 \times 4,096$ configuration space sampling interpolation to $8,192 \times 8,192$ samples was needed. Applying the propagation operator to fields that are not adequately sampled for phase unwrapping eliminates fine detail but does not otherwise affect the simulations. The fact that the diffraction-free path-integrated phase was undersampled was a consequence of the very large but representative phase variations associated with the configuration-space realizations. MPS simulations typically limit the large-scale phase variations that map directly onto the complex field phase as total electron content structure unaffected by diffraction.

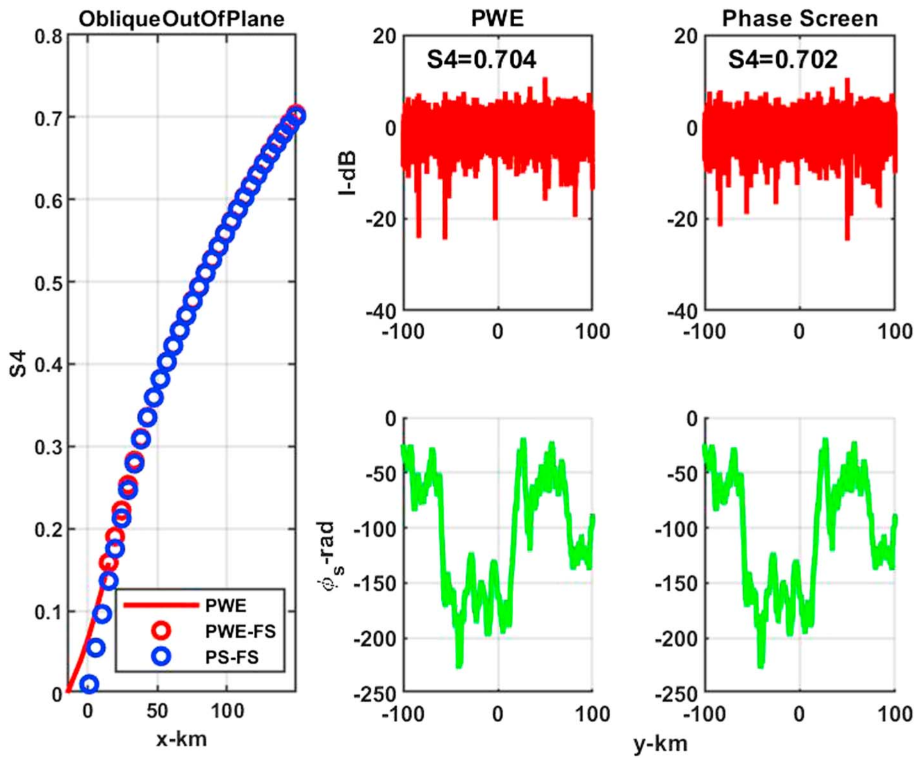

Figure 5. Oblique out-of-plane summary. Same format as Figure 3.

3.1. Structure Evolution and Phase-Screen Equivalence

Four realizations with different magnetic field orientations were generated for this study. Using the polar angles defined in Appendix A, the realizations will be referred to as cross field ($\theta_b = 90°, \psi_b = -90°$); oblique in-plane ($\theta_b = 60°$, $\psi_b = -90°$); oblique out-of-plane ($\theta_b = 45°$, $\psi_b = -60°$); and field aligned ($\psi = 0°$). Intensity moments provide measures of the signal intensity scintillation. With $I(x, \vec{\rho}) = |\psi(x, \vec{\rho})|^2$, fractional moments are defined as

$$F_m(x) =< I(x, \vec{\rho})^m > / < I(x, \vec{\rho})>^m \text{for } m = 1, 2, 3, \ldots . \quad (22)$$

The PWE conserves signal intensity, whereby $< I(x, \vec{\rho}) >= 1$. The $S4$ index is computed as $S4(x) = \sqrt{F_2(x) - 1}$. The complex field $\psi_y(x, y) = \psi(x, y, 0)$ is used as a surrogate for one-dimensional measurements. The intensity of $\psi_y(x, y)$ follows directly. The phase of the complex field scan must be *unwrapped*.

Figures 3–6 summarize the structure evolution. The left frames of each figure summarize the $S4$ evolution. The solid red curves from $x = -15$ km to $x = 15$ km are derived from PWE integration. The red circles beyond $x = 15$ km are derived from free-space propagation of the PWE field. The blue circles, which start at $x = 0$ with zero intensity, are derived from the free-space propagation of the phase-screen fields. The upper plots in the two right frames show the intensity of one-dimensional scans at $z = 0$ in the observation-plane fields at 150 km. The center frames are from PWE integrations. The right frames are propagated from an equivalent phase-screen at $x = 0$.

The lower frames summarize the unwrapped phase of the one-dimensional scans at $z = 0$ (red), with the path-integrated phase overlaid (green) as a reference. As already noted, the large phase excursions reflect the configuration-space realizations. With interpolated sampling the path-integrated phase $\phi(\vec{\rho})$ can be recovered from $\psi(\vec{\rho}) = \exp\{i\phi(\vec{\rho})\}$. Strictly speaking, solutions to the PWE will not generate a phase discontinuity, as would occur from a surface reflection. However, the complex field structure will ultimately induce errors in the phase unwrapping operation. Even so, the recovered phase structure is almost hidden with the resolution of the summary plots. Phase scintillation with be discussed below.

The main result here is the striking statistical similarity of the PWE and phase-screen intensity realizations independent of the propagation direction relative to the magnetic field. This is particularly interesting with

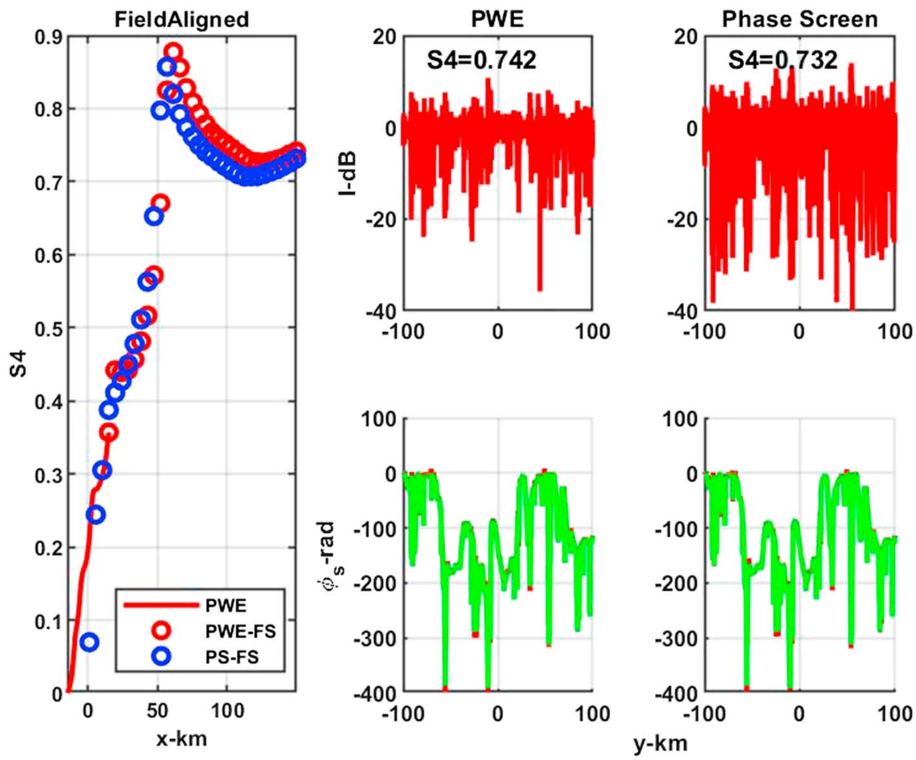

Figure 6. Oblique field-aligned summary. Same format as Figure 3.

regard to the field-aligned realization, which shows *strong focusing* indicated by the $S4$ peak in Figure 6. This is a well-known property of propagation in continuous-fractal power law structure. The associated field structure was as *diffractals* by Berry (1979). However, it is problematic that such structures would be observed in nature because they depend critically on the unvarying cylindrical structure of the striations. The upper frame of Figure 7 shows a color display of the decibel field-aligned intensity variation at $x = 150$ km. The lower frame is a zoomed region near the center of the display to illustrate the complexity of the field structure.

3.2. Propagation Diagnostics

Propagation diagnostics address the question of how one-dimensional measurements can be processed to estimate the ionospheric structure model parameters that define (20). Invoking phase-screen equivalence, the complex fields are initiated by path-integrals scaled to phase. TEC is formally a mapping of the three-dimensional electron density onto a reference plane:

$$\Delta TEC(\vec{\rho}) = \int_0^L \Delta N_e(x, \vec{\rho})\mathrm{d}x. \tag{23}$$

Tomographic and data fusion methods can recover large-scale ionospheric structure from multiple TEC measurements. Stochastic TEC structure is generally treated as noise. For stochastic TEC diagnostics the following SDF transformation are used:

$$\Phi^{(2)}_{\Delta\mathrm{TEC}}\left(\vec{\kappa}\right) = L\int \frac{\sin^2(\kappa_x L/2)}{(\kappa_x L/2)^2}\Phi_{N_e}(\kappa_x, \kappa_y, \kappa_z)\frac{d\kappa_x}{2\pi} \tag{24}$$

$$\Phi^{(1)}_{\Delta\mathrm{TEC}}\left(\kappa_y\right) = L\int\int \frac{\sin^2(\kappa_x L/2)}{(\kappa_x L/2)^2}\Phi_{N_e}(\kappa_x, \kappa_y, \kappa_z)\frac{d\kappa_x}{2\pi}\frac{d\kappa_z}{2\pi} \tag{25}$$

The structure model (20) can be used to generate high-resolution calculations of $\Phi_{N_e}(\kappa_x, \kappa_y, \kappa_z)$. High-resolution is necessary to capture the singular behavior of the field-aligned structure. Numerical integrations are then used to compute the one-dimensional SDFs (24) and (25). The results are summarized

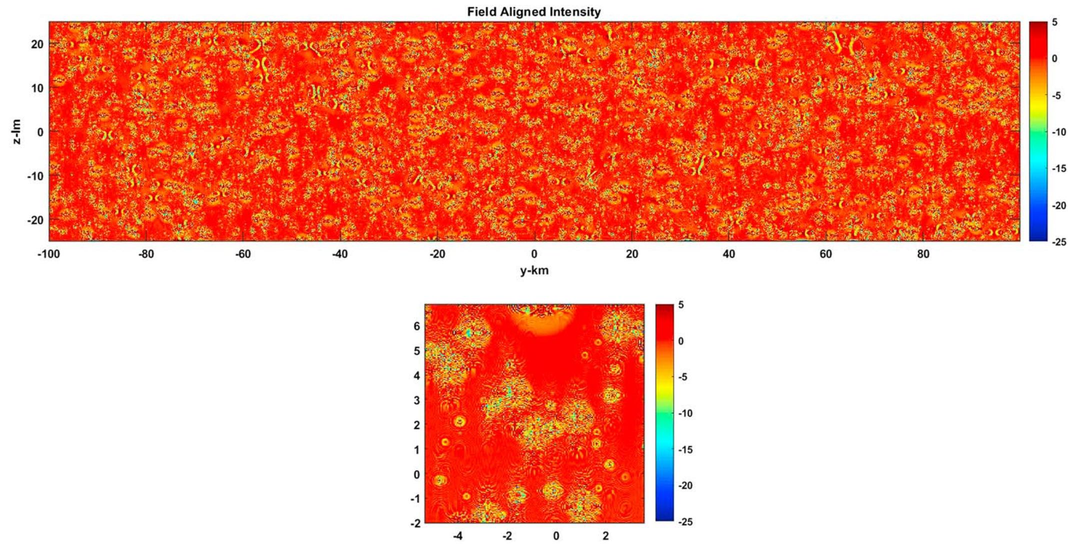

Figure 7. Field-aligned decibel intensity variation (upper frame) with zoomed central region (lower frame).

in Figure 8. The four geometries for the configuration-space realizations were used with an additional propagation path offset by 1° from strict cross-field propagation. The upper frame summarizes the in situ one-dimensional SDFs for the five geometries with the one-dimensional SDF 19 overlaid in magenta. There is no geometric sensitivity to one-dimensional in situ measurements.

The lower frame in (8) shows the TEC results. The results are nearly identical to the in situ SDFs with the exceptions of the cross-field and near-cross-field geometries. The $\sin^2(\kappa_x L/2)/(\kappa_x L/2)^2$ weighting only affects the result when the spectral intensity variation with κ_z is resolved and confined to $\kappa_z = 0$. The prediction is verified in Figure 6 of Rino et al. (2018). At the time that paper was written, no confirming calculations were available.

There is an analytic theory that characterizes the intensity SDF initiated by the stochastic TEC upon conversion to phase:

$$\Phi_I\left(\vec{\kappa}\right) = \int\int \left[\exp\left\{-Lk^2 g\left(\vec{\alpha}, \vec{\kappa}\rho_F^2\right)\right\} - 1\right] \exp\left\{-i\vec{\kappa}\cdot\vec{\alpha}\right\} d\vec{\alpha}. \quad (26)$$

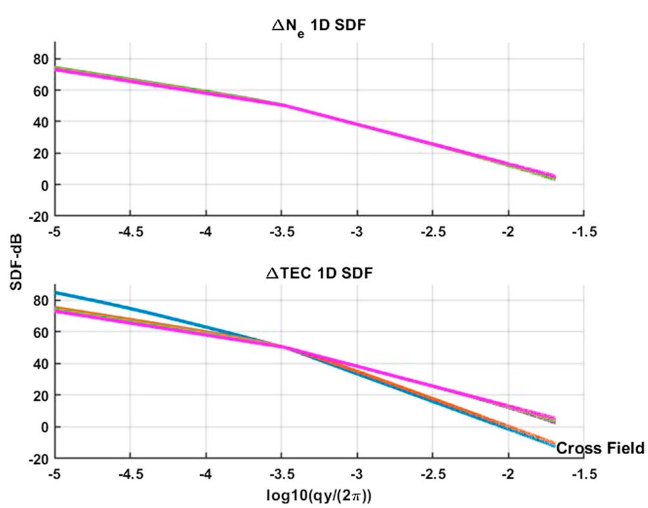

Figure 8. The upper frame shows numerical calculations of one-dimensional in situ SDFs. The lower frame shows numerical calculations of one-dimensional TEC SDFs, which are potentially effected by the path integration. Four geometries were used for each set of calculations. The magenta overlay is the target one-dimensional SDF. The only departure from the target SDF is for the two cases within 1° of cross-field propagation identified in the lower frame. SDF = spectral density function.

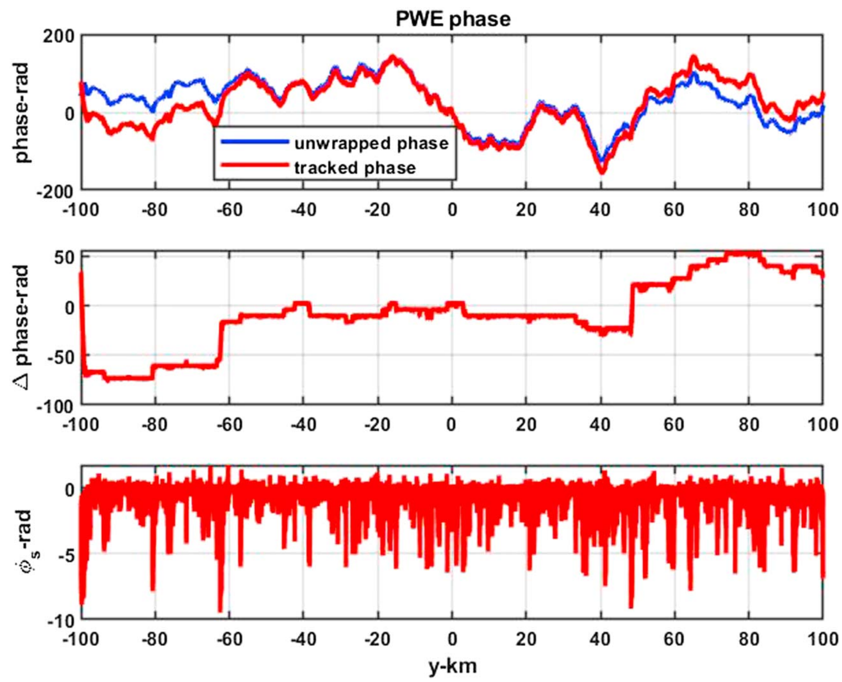

Figure 9. Upper frame is cross-field intensity at $x = 150$ km. Lower frame is difference between unwrapped phase and total electron content reference phase. PWE = parabolic wave equation.

where

$$g\left(\vec{\alpha}_1, \vec{\alpha}_2\right) = 8k^2 \int\int \Phi_{\Delta\phi}(\vec{\kappa})\sin^2\left(\vec{\kappa}\cdot\vec{\alpha}_1/2\right)\sin^2\left(\vec{\kappa}\cdot\vec{\alpha}_2/2\right)\mathrm{d}\kappa/(2\pi)^2, \tag{27}$$

and

$$SI^2 = \int\int \Phi_I(\vec{\kappa})\mathrm{d}\vec{\kappa}/(2\pi)^2. \tag{28}$$

Calculation of $\Phi_I\left(\vec{\kappa}\right)$ requires a nested double integration together with an analytic computation of the path-integrated phase. At the present time there is no tractable means of using these results directly for interpreting intensity scintillation diagnostics.

The two-dimensional theory is formally obtained from (26) and (27) with the replacement

$$\Phi_{\Delta\phi}(\vec{\kappa}) = 2\pi\delta(\kappa_z)\Phi_{\Delta\phi}(\kappa_y). \tag{29}$$

The result is strictly applicable to cross-field realizations. However, the theory is applied commonly to the structure in the two-dimensional propagation plane that contains the propagation vector. A complete evaluation of the limitations of the two-dimensional model would require comparisons of the results as the scintillation develops, which is beyond the scope of the current study.

Under strong scintillation conditions, the simulated phase structure is important because it is used directly in simulators for GNSS performance evaluation. Whereas the fully three-dimensional model is resolution limited, two-dimensional models can generate high-resolution signal realizations efficiently. A recent model with connections to earlier models is described in Rino et al. (2018). The three-dimensional PWE simulations serve mainly for validation, which will be pursued directly in section 3.3. To explore the phase structure, Figure 9 is a expanded plot of the middle frame cross-field-in-plane summary in Figure 3. The TEC reference phase has been subtracted from the recovered field phase, which is effectively a definition of phase scintillation. The large phase transitions here are due to unwrapping errors, but similar phase transitions are observed in measured signal phase. The key point to note here is that if the data were realigned to remove what are clearly unresolved phase transitions, the residual phase structure would be a small fraction of the TEC reference, even though the $S4$ index is near unity.

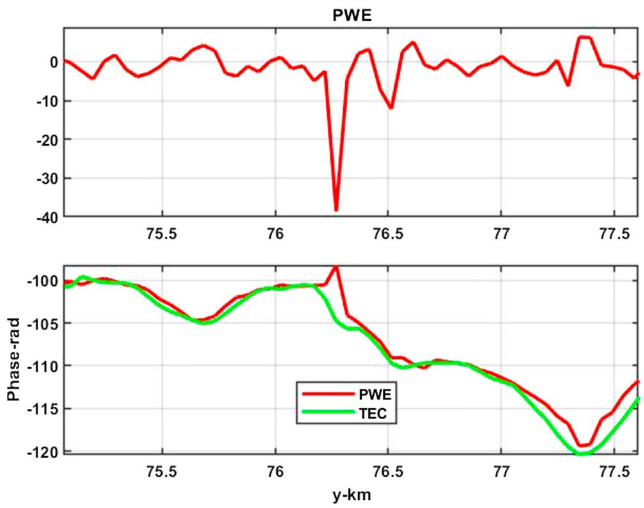

Figure 10. Zoomed intensity and scintillation phase associated with deep oblique-out-of-plane realization summarized in Figure 5. PWE = parabolic wave equation. TEC = total electron content.

Figure 10 shows a zoomed view of the intensity and phase variation for a deep fade in the oblique-out-of-plane realization summarized in Figure 5. The rapid phase change associated with the deep fade reflects the canonical structure described in Humphreys et al. (2010). The three-dimensional oblique geometries generate intricate complex field structure. The suggests that aside from the phase unwrapping errors, the field structure is representative. The canonical fade is not unique to cross-field geometries.

3.3. Two-Dimensional Propagation

The free-space propagation operation is its own inverse with the sign of the Fresnel factor reversed. Moreover, to the extent that phase-screen equivalence applies, iterative back propagation to minimize the intensity structure should recover the equivalent phase-screen field, which ideally has no intensity variation. The problem is only one-dimensional scans of an observed complex field are measurable. Back propagation generally refers to applications of the two-dimensional form of (4):

$$\Theta\psi\,(x;y) = \int \hat{\psi}\,(x;\kappa)\exp\left\{i\kappa^2 x_p/(2k)\right\}\exp\left\{iy\kappa\right\}\frac{d\kappa}{2\pi}. \qquad (30)$$

Successful removal of the intensity scintillation identifies the location of the equivalent phase screen and potentially recovers the path-integrated phase structure. Regarding necessity, two-dimensional propagation models are used extensively for modeling atmospheric effects such as ducting and surface reflections. Model validation is determined by how well the model predictions match transmission data. Iterative application of the two-dimensional back propagation operator is readily applied to one-dimensional scans of ionospheric diagnostic measurements (Kuttler & Dockery, 1991).

Figure 11 shows the backpropagated intensity and phase derived from the cross-field simulation. The backpropagation distance and minimum $S4$ are listed in the upper frame. The small errors are attributed to the differences between the PWE fields and the equivalent phase-screen fields. Figure 12 shows the back propa-

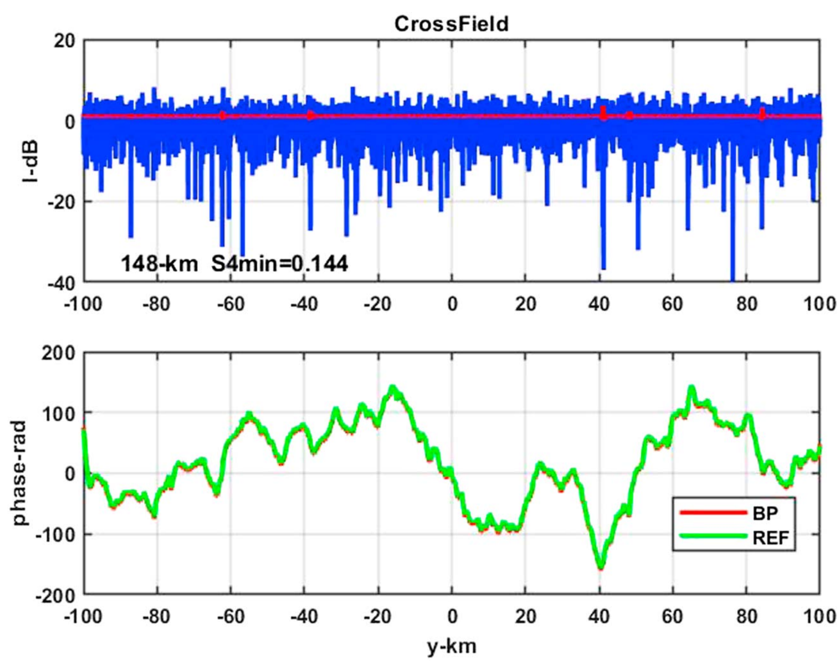

Figure 11. Upper frame shows cross-field intensity scan in measurement plane at 150 km (blue) with backpropagated intensity overlaid (red). The minimum distance and $S4$ are listed in the figure. The lower frame shows the backpropagated (blue) and total electron content (green) phase.

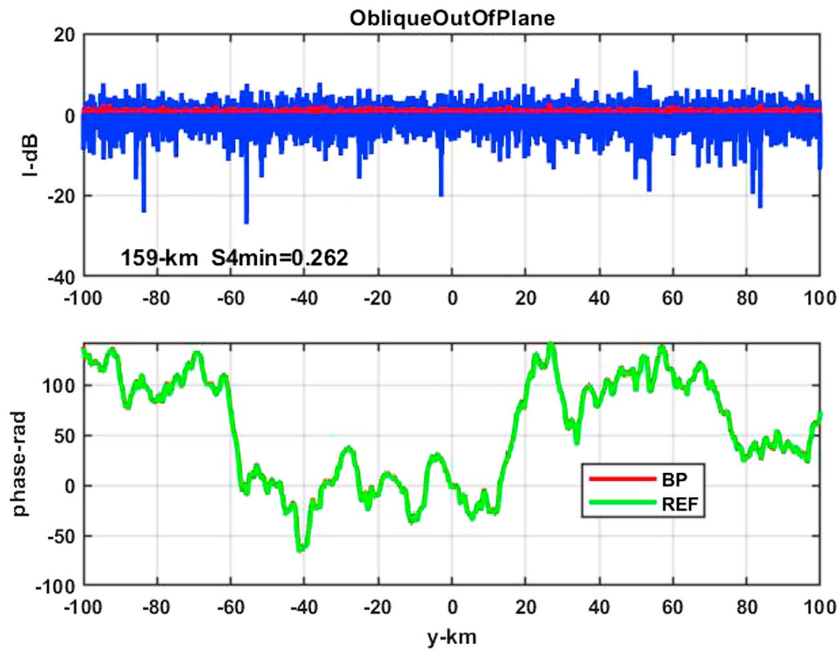

Figure 12. Same display as Figure 11 for oblique-out-of-Plane geometry.

gated intensity and phase derived from the oblique-out-of-Plane simulation. As expected, there is increased degradation of backpropagation recovery as the propagation angle relative to the magnetic field decreases. As already noted, the diffraction-induced phase changes are a small fraction of the TEC phase. When applied to field-aligned structure realization $S4_{\mathrm{min}} = 0.58$. Two-dimensional backpropagation would not be expected to effective when applied to scans of isotropic EM fields.

4. Summary and Discussion

This paper used PWE simulations with configuration-space realizations to explore propagation in extended highly anisotropic media as presented by the Earth's ionosphere. The principal result is illustrated in Figures 3–6. The remote effects of the cumulative interaction of an EM wave with anisotropic structure is statistically equivalent to the free-space propagation from a phase centered in the structured region. Although detectable scintillation is present as the EM wave exits the disturbed region, statistical phase-screen equivalence is achieved at propagation distances equal to the extend of the intercepted structure.

Configuration-space realizations were used to generate structure realizations for split-step integration of the PWE. We extended the one-dimensional SDF characterization in the original paper (equation (19) in this paper) to an analytic isotropic two-dimensional characterization of the ionospheric structure in cross-field planes. Purely geometric transformations, (14) generate a simply parameterized three-dimensional ionospheric structure model defined by (20). We then showed that one-dimensional or in situ measurements could be processed to determine the defining ionospheric model parameters subject to time-to-space conversion.

Regarding the field structure, we showed that the phase of the complex field is dominated by the TEC component mapped directly onto the signal phase. The phase structure generated by diffraction is a small fraction of the TEC component. This suggests that TEC structure can be measured directly, for example by using the IPE procedure described in (Rino & Carrano, 2018) to estimate model parameters, which is being pursued.

The complete interpretation of scintillation diagnostics would require the evaluation of theoretical results represented by (26) and (27). The computational requirements preclude direct applications at this time. However, the successful use of theories based on tractable two-dimensional propagation models could be evaluated by backpropagation as a sufficient but not strictly necessary condition. The results shows that back propagation is effective for non-field-aligned propagation. Backpropagation to the equivalent phase-screen structure indirectly supports the IPE procedure for estimating the power law parameters from measured intensity SDFs.

The ultimate objective is to demonstrate procedures that can be applied efficiently enough to process the very large volumes of ionospheric diagnostic data that are being accumulated. The study by Wernik et al. (1980) is exemplary. The results in this paper support TEC IPE analysis under weak to moderate scintillation conditions with IPE applied to intensity analysis for moderate to strong scintillation.

Appendix A: Rotation Matrix

Let $\vec{u}_b$ represent a unit vector along the magnetic field direction in the data space coordinate system. In terms of polar angles

$$\vec{u}_b = [\cos(\theta_b), \sin(\theta_b)\cos(\phi_b), \sin(\theta_b)\sin(\phi_b)]. \tag{A1}$$

The 3×3 matrix$C$ that transform $C\vec{u}_b$ to a unit vector rotates a vector in the data space to a field-aligned coordinate system with principal axes aligned with $\vec{u}_b$. The elements are

$$c_{11} = \cos(\theta) \tag{A2}$$

$$c_{12} = \sin(\theta)\cos(\psi) \tag{A3}$$

$$c_{13} = \sin(\theta)\sin(\psi) \tag{A4}$$

$$c_{21} = -\sin(\theta) \tag{A5}$$

$$c_{22} = \cos(\theta)\cos(\psi) \tag{A6}$$

$$c_{23} = \cos(\theta)\sin(\psi) \tag{A7}$$

$$c_{31} = -\sin(\psi) \tag{A8}$$

$$c_{32} = \cos(\psi) \tag{A9}$$

$$c_{23} = 0 \tag{A10}$$

Acknowledgments
All of the data in this paper are simulations that can be reproduced as described in the paper. Constructing configuration-space realizations is described in Rino et al. (2018). The reported research was supported in part by AFRL Contract FA9453-12-C-0205, “ADVANCED DATA DRIVEN SPECIFICATION AND FORECAST MODELS FOR THE IONOSPHERE-THERMOSPHERE SYSTEM.”

References

Béniguel, Y. (2002). Global Ionospheric Propagation Model (GIM): A propagation model for scintillations of transmitted signals. *Radio Science*, *37*(3), 1032. https://doi.org/10.1029/2000RS002393

Berry, M. V. (1979). Diffractals. *Journal of Physics A: Mathematical and General*, *12*(6), 781–797.

Bilitza, D., & Reinisch, B. (2015). International Reference Ionosphere 2007: Improvements and new parameters. *Advances in Space Research*, *42*, 599–609.

Booker, H. G., Ratcliffe, J. A., & Shinn, D. H. (1950). Diffraction from an irregular screen with applications to ionospheric problems. *Proceedings of the Cambridge Philosophical Society*, *242 A*, 579–607.

Briggs, B. H., & Parkin, I. A. (1962). On the variation of radio star and satellite scintillations with zenith angle. *Journal of Atmospheric and Solar-Terrestrial Physics*, *25*, 339–365.

Budden, K. G. (1964). The amplitude fluctuations of the radio wave scattered from a thick ionospheric layer with weak irregularities. *Journal of Atmospheric and Solar-Terrestrial Physics*, *27*, 155–172.

Carrano, C., Groves, K., Delay, S., & Doherty, P. (2014). An inverse diffraction technique for scaling measurements of ionospheric scintillations on the GPS L1, L2, and L5 carriers to other frequencies. Proceedings of the 2014 Institute of Navigation ION ITM Meeting San Diego, Calif., Institute of Navigation.

Carrano, C., & Rino, C. (2016). A theory of scintillation for two-component power law irregularity spectra: Overview and numerical results. *Radio Science*, *51*, 789–813. https://doi.org/10.1002/2015RS005903

Carrano, C. S., Rino, C. L., & Groves. (2017). Maximum likelihood estimation of phase screen parameters from ionospheric scintillation spectra. In *15th International Ionospheric Effects Symposium,Alexandria, VA, May 9-11*, pp. 1–11.

Deshpande, K. B., Bust, G. S., Clauer, C. R., Rino, C. L., & Carrano, C. S. (2014). Satellite-beacon Ionospheric-scintillation GlobalModel of the upper Atmosphere (SIGMA) I: High-latitude sensitivity study of the model parameters. *Journal of Geophysical Research: Space Physics*, *119*, 4026–4043. https://doi.org/10.1002/2013JA019699

Ghafoori, F., & Skone, S. (2015). Impact of equatorial ionospheric irregularities on GNSS receivers using real and synthetic scintillation signals. *Radio Science*, *50*, 294–317. https://doi.org/10.1002/2014RS005513

Gherm, V. E., & Zernov, N. N. (2015). Strong scintillation of GNSS signals in the inhomogeneous ionosphere: 2. Simulator of transionospheric channel. *Radio Science*, *50*, 168–176. https://doi.org/10.1002/2014RS005604

Gherm, V. E., & Zernov, N. N. (2017). Extension of hybrid scintillation propagation model to the case of field propagation in the ionosphere with highly anisotropic irregularities. *Radio Science*, *52*, 874–883. https://doi.org/10.1002/2017RS006264

Gherm, V. E., Zernov, N. N., & Strangeways, H. (2005). Propagation model for transionospheric fluctuational paths of propagation: Simulator of the transionospheric channel. *Radio Science*, *40*, RS1003. https://doi.org/10.1029/2004RS003097

Ghiglia, D. C., & Pritt, M. D. (1998). *Two-dimensional phase unwrapping theory, algorithms, and software*. New York: John Wiley & Sons, Inc.

Humphreys, T. E., Psiaki, M. L., Ledvina, B. M., Cerruti, A. P., & Kintner, P. M. (2010). Data-driven testbed for evaluating GPS carrier tracking loops in ionospheric scintillation. *IEEE Transactions on Aerospace and Electronic Systems*, *46*(4), 1609–1623.

Knepp, D. L. (1983). Multiple phase-screen calculation of the temporal behavior of stochastic waves. *Radio Science*, *71*(6), 722–737.

Kuttler, J., & Dockery, G. (1991). Theoretical description of the parabolic approximation/ Fourier split-step method of representing electromagnetic propagation in the troposphere. *Radio Science*, *26*, 381–393.

Retterer, J. M. (2010). *Journal of Geophysical Research*, *115*, A03307. https://doi.org/10.1029/2008JA013840

Rino, C., Briestch, B., Morton, Y., Jiao, Y., Xu, D., & Carrano, C. (2018). A Compact multifrequency GNSS scintillation model. *Institute of Navigation Journal*, *65*, 563–569. https://doi.org/10.1002/navi.263

Rino, C. L., & Carrano, C. S. (2018). On the characterization of intermediate-scale ionospheric structure. *Radio Science*, *53*, 1316–1327. https://doi.org/10.1029/2018RS006709

Rino, C., Carrano, C., Groves, K., & Yokoyama, T. (2018). A configuration space model for intermediate-scale ionospheric structure. *Radio Science*, *53*, 1472–1480. https://doi.org/10.1029/2018RS006678

Rino, C., Yokoyama, T., & Carrano, C. (2018). Dynamic spectral characteristics of high-resolution simulated equatorial plasma bubbles. *Progress in Earth and Planetary Science*, *5*, 83. https://doi.org/10.1186/s40645-018-0243-0

Rino, C. L. (2011). *The theory of scinillation with applications in remote sensing*. New York: Wiley.

Secan, J. A., Bussey, R. M., Fremouw, E. J., & Basu, S. (1995). An improved model of equatorial scintillation. *Radio Science*, *30*(3), 607–617.

Tatarskii, V. I. (1971). *The effects of the turbulent atmosphere on wave propagation*. Springfield, VA: National Technical Information Service.

Tsai, L. C., Cheng, K. C., & Liu, C. H. (2011). GPS radio occultation measurements of ionospheric electron density from low Earth orbit. *Journal of Geodesy*, *85*, 7421–7428.

Wernik, A. W., Liu, C. H., & Yeh, K. C. (1980). Model computations of radio wave scintillation caused by 892 equatorial ionospheric plasma bubbles. *Radio Science*, *15*, 559–572.

Zernov, N. N., & Gherm, V. E. (2015). Strong scintillation of GNSS signals in the inhomogeneous ionosphere. 1: Theoretical background. *Radio Science*, *50*, 153–167. https://doi.org/10.1002/2014RS005603